

Article

Rational A/B Site Ion Doping to Design Efficient and Stable $\text{Pr}_{0.5}\text{Ba}_{0.4}\text{Ca}_{0.1}\text{Fe}_{1-x}\text{Co}_x\text{O}_{3-\delta}$ Perovskites as Zinc–Air Batteries Cathode

Kaixin Li , Zhanhua Dong and Zhe Lü * 

School of Physics, Harbin Institute of Technology, 92 Xi Dazhi Street, Harbin 150001, China

* Correspondence: lvzhe@hit.edu.cn

Abstract: The development of robust and efficient electrocatalysts for use in fuel cells and metal–air batteries has garnered a great deal of interest due to the quest for clean and renewable energy sources. In this paper, a promising Co-doped $\text{Pr}_{0.5}\text{Ba}_{0.4}\text{Ca}_{0.1}\text{Fe}_{1-x}\text{Co}_x\text{O}_{3-\delta}$ ($x = 0, 0.2, 0.4, 0.6, 0.8$; denoted as PBCFC- x , $x = 0, 2, 4, 6, 8$) with enhanced durability and electrocatalytic ORR/OER activity for zinc–air battery cathode catalysts is presented. Particularly, PBCFC-6 exhibits the best bifunctional catalytic activity in alkaline media among several materials, according to research using the RDE. The zinc–air battery with PBCFC-6 as the cathode catalyst delivered the smallest discharge–charge voltage difference at the current density of $10 \text{ mA}\cdot\text{cm}^{-2}$ and only increased by 0.031 V after 220 cycles (220 h), demonstrating its superior bifunctional catalytic activity and durability. The optimized electrochemical performance of both OER and ORR as well as stability in zinc–air batteries might result from the higher electrical conductivity, increasing concentration of adsorbed oxygen, and the greater proportion of Fe^{4+} ($t_{2g}^3e_g^1$) with optimal electron occupancy, owing to the partial replacement of Fe with Co.

**Citation:** Li, K.; Dong, Z.; Lü, Z.

Rational A/B Site Ion Doping to

Design Efficient and Stable

 $\text{Pr}_{0.5}\text{Ba}_{0.4}\text{Ca}_{0.1}\text{Fe}_{1-x}\text{Co}_x\text{O}_{3-\delta}$

Perovskites as Zinc–Air Batteries

Cathode. *Batteries* **2022**, *8*, 259.[https://doi.org/10.3390/](https://doi.org/10.3390/batteries8120259)[batteries8120259](https://doi.org/10.3390/batteries8120259)

Academic Editor: Carlos Ziebert

Received: 21 October 2022

Accepted: 25 November 2022

Published: 28 November 2022

Publisher's Note: MDPI stays neutral with regard to jurisdictional claims in published maps and institutional affiliations.

**Copyright:** © 2022 by the authors.

Licensee MDPI, Basel, Switzerland.

This article is an open access article

distributed under the terms and

conditions of the Creative Commons

Attribution (CC BY) license ([https://](https://creativecommons.org/licenses/by/4.0/)[creativecommons.org/licenses/by/](https://creativecommons.org/licenses/by/4.0/)

4.0/).

Keywords: $\text{Pr}_{0.5}\text{Ba}_{0.4}\text{Ca}_{0.1}\text{Fe}_{1-x}\text{Co}_x\text{O}_{3-\delta}$; rechargeable zinc–air batteries; ORR/OER; bifunctional catalyst

1. Introduction

Given the complicated global situation and the ongoing depletion of fossil energy sources, there is urgency in researching and developing sustainable and environmentally friendly conversion and storage devices, such as fuel cells and metal–air batteries [1–11]. A growing number of studies on zinc–air batteries have been conducted due to their superior chemical reversibility and greater safety compared to other types of metal–air batteries. The study and innovation of air electrode catalysts for zinc–air batteries are mainly centered on the oxygen reduction reaction (ORR) and oxygen evolution reaction (OER) [12–15]. Until now, the best materials for OER/ORR catalysis have been the noble metals represented by Pt/C and RuO_2 , etc. [8]. However, the limited stability, poor catalytic efficacy, and expensive price of precious metal materials prevent their wider application [16–18]. Thanks to the flexibility of the B-site and A-site cations and the O-site anion, ABO_3 -type perovskites typically exhibit a variety of structural and physicochemical features [19–25]. In addition, given their relatively low cost and abundant deposits, they are anticipated to take the replacement of precious metal catalysts in zinc–air battery cathode catalysts [20,26–29]. Therefore, to handle the obstacles of sluggish ORR and OER kinetics and facilitate the commercial scale-up of zinc–air batteries, it is vital to develop low-cost perovskite catalysts with excellent catalytic performance and durability.

Alexis et al. reported a range of $(\text{Ln}_{0.5}\text{Ba}_{0.5})\text{CoO}_{3-\delta}$ ($\text{Ln} = \text{Sm}, \text{Pr}, \text{Ho}, \text{and Gd}$) as OER high-activity catalysts, with samples where Pr was present in the Ln position demonstrating the best performance [30]. Numerous researchers have studied the $\text{Pr}_{0.5}\text{Ba}_{0.5}\text{CoO}_{3-\delta}$ -based perovskite extensively using surface modification, ion doping, and nanosizing [31–37].

He et al. reported that minimal doping of Ca increases the corrosion resistance of perovskite oxides by preventing Ba leaching and surface degradation, thereby improving their structural stability to provide enduring OER performance [38]. According to Li et al., the Co-Fe of $\text{BaCo}_{0.4}\text{Fe}_{0.4}\text{Zr}_{0.1}\text{Y}_{0.1}\text{O}_{3-\delta}$ doped with Co ions at the B-site would have lower defect formation energy, modulating its oxygen vacancy concentration and enhancing its catalytic activity [39]. Due to their affordable price and acceptable catalytic activity, Fe-based perovskites have drawn a lot of attention lately [34,40–43]. Since the lower electrical conductivity of Fe-based perovskites is not favorable for charge transfers during catalytic reactions, their catalytic activity is relatively poor compared to that of Co-based perovskites. Previously, the bifunctional catalytic activity of $\text{PrFeO}_{3-\delta}$ -based perovskites has been poorly investigated. Therefore, a thorough understanding of the characteristics of $\text{PrFeO}_{3-\delta}$ -based perovskites is crucial to enhance their bifunctional catalytic activity through rational design.

Herein, we designed a series of PBCFC- x ($x = 0, 2, 4, 6, 8$) by a citrate–nitrate combustion process with trace Ca ion doping at the A-site and Co ion substitution at the B-site to probe the highly catalytically active and durable perovskite oxides. The catalytic activity of the obtained catalyst materials was then investigated in 0.1 M KOH solution. The aforementioned materials' physicochemical characteristics, including surface shape, crystal structure, surface species, and elemental valence, were investigated using XRD, SEM, EDS, and XPS to figure out the altered ORR/OER activity. Additionally, the bifunctional catalytic performance and the durability of a series of perovskite materials as cathode catalysts was evaluated via a homemade zinc–air battery at room temperature in constant current discharge and long-term cycle tests.

2. Experimental Section

2.1. The Synthesis of Material

A range of PBCFC- x ($x = 0, 2, 4, 6, 8$) perovskite materials was prepared by applying the citrate–nitrate combustion process. All drugs were analytically pure from Aladdin and were not further purified before conducting the experiments. First, in order of ease of dissolution, specific amounts of Pr_6O_{11} , $\text{Ba}(\text{CO}_3)_2$, $\text{Ca}(\text{CO}_3)_2$, $\text{Fe}(\text{NO}_3)_3 \cdot 9\text{H}_2\text{O}$, and $\text{Co}(\text{NO}_3)_2 \cdot 6\text{H}_2\text{O}$ were dissolved in a vigorously magnetically stirred dilute nitric acid solution. Citric acid and ethylenediaminetetraacetic acid were added as complexing agents in a 1:2:1 ratio of AC: EDTA: metal ions and the solution's pH was controlled at around 7 by the addition of ammonia dropwise. The solution was stirred in a 60 °C water bath for 24 h until the metal cations were fully complex. The complexed solution was then heated on an evaporating dish in an electric furnace until spontaneous combustion of the precursors was obtained. The precursors were heated to 900 °C for 5 h and annealed at a rate of 2 °C/min under air conditions to obtain the corresponding perovskite materials.

2.2. Characterizations

The purity and crystal structures of perovskite catalysts were determined over the scanning angular range of 10° to 90° by X-ray diffraction (XRD, 40 kV and 15 mA, $\lambda = 1.5418 \text{ \AA}$, Cu-K α radiation, PANalytical Aeris, Melbourne, Australia). The field emission scanning electron microscope (SEM, Hitachi S-4800, Tokyo, Japan) equipped with energy dispersive X-ray spectroscopy (EDS) was performed to deeply examine the elemental composition and surface morphology of the as-prepared catalysts. The Brunauer–Emmett–Teller (BET, ASAP2460, Norcross, GA, USA) method was used to determine the specific surface area of the prepared perovskite oxides. The surface cation valence states and oxygen-related species were explored using X-ray photoelectron spectroscopy (XPS, Al K α radiation, AXIS-His spectrometer, Waltham, MA, USA). The measured XPS binding energy was calibrated regarding the peak of the standard C 1s at 284.8 eV. To examine the as-prepared material's conductivity, the PBCFC- x samples were pressed into strips and sintered in an air atmosphere at 1100 °C for 10 h to ensure their denseness and were tested at room temperature using the four-probe method.

2.3. Electrochemical Measurements

To make the uniform electrocatalyst slurry, 5 mg of conductive carbon black (XC72R), 5 mg of catalyst, and 50 μL of Nafion solution (5 wt %) were added to a mixture of isopropanol (400 μL) and deionized water (100 μL), followed by sonication for 2 h. The homogenized slurry was then transferred in 5 μL to a polished glassy carbon (GC, 0.196 cm^2 area) electrode and allowed to dry at room temperature for an entire night, with a catalyst loading of 0.232 $\text{mg}\cdot\text{cm}^{-2}$. In addition, commercially available Pt/C (20 wt.%) and IrO₂ were tested using the same preparation process as a reference catalyst.

The ORR and OER tests were carried out using rotating disc electrodes (RDE) in a three-electrode system. A Pt wire, GC electrodes coated with catalyst films, and SCE were employed as the counter, the work, and the reference electrodes. All electrochemical tests were performed using the CHI760E electrochemical station in an O₂-saturated 0.1M KOH aqueous solution at room temperature. It should be mentioned that all potentials tested vs. SCE were handled with IR corrected and converted to the potential vs. RHE. The LSV (1600 rpm, 10 $\text{mV}\cdot\text{s}^{-1}$) for OER and ORR was recorded over a potential range of 0 to 1 V and -0.9 to 0.2 V (vs. SEC), respectively. It is necessary to maintain oxygen saturation in the electrolyte utilized during the ORR and OER test.

The following Koutecky–Levich (K–L) equation was employed to determine the electron transfer number to examine the dominated pathway in ORR of the as-prepared perovskite materials [42]:

$$j = \frac{1}{j_k} + \frac{1}{j_l} = \frac{1}{j_k} + \frac{1}{B\omega^{\frac{1}{2}}} = \frac{1}{j_k} + \frac{1}{0.62nFC_{O_2}D_{O_2}^{\frac{2}{3}}\nu^{-\frac{1}{6}}\omega^{\frac{1}{2}}} \quad (1)$$

where, j , j_k , and j_l in the above equations respond to the measured, kinetic, and diffusion-limiting current density, respectively. ν , F , ω , D_{O_2} , n , and C_{O_2} are the kinetic viscosity of 0.1 M KOH solution, Faraday constant, rotating rate, the diffusion coefficient of oxygen, electron transfer number, and saturated bulk concentration of oxygen, respectively.

2.4. Characterization and Preparation of Zinc–Air Batteries

To evaluate both the stability and catalytic performance of as-prepared materials as cathode catalysts under practical working conditions, a homemade zinc–air battery was assembled. To prepare the catalytic layer for the air electrode, a mixture of acetylene black (Li-2060): catalyst: activated carbon (YP50F): polytetrafluoroethylene emulsion (PTFE, 60 wt%, teflon) at a ratio of 1:3:3:3 was stirred vigorously in alcohol for at least 3 h to produce a homogeneous suspension. The homogeneous mixture was then loaded to one side of the flattened nickel foam after being dried to a gel-like solid at 80 °C, resulting in a loading of approximately 5 $\text{mg}\cdot\text{cm}^{-2}$ (only perovskite). The gas diffusion layer was coated to another side of the nickel foam, except that the weight ratio of PTFE: acetylene black was 7:3. The area of the positive and negative electrodes were 4 cm^2 and 6.25 cm^2 , respectively. To realize the durability and the catalytic properties of the prepared samples, a cycle (30 min for discharge, 30 min for charge) and constant current discharge experiment was carried out at room temperature for zinc–air batteries with different perovskite oxides as air electrode catalysts. There are some differences between the negative electrode and electrolyte used in homemade rechargeable and primary zinc–air batteries. The former uses 1 mm thick polished zinc flakes and a 6M KOH + 0.2M zinc acetate solution, while the latter uses zinc powder pressed into flakes and a 6M KOH solution. Both constant current discharge and cycling tests of the batteries were carried out at a current density of 10 $\text{mA}\cdot\text{cm}^{-2}$ using the NEWARE battery system (Fujian, China).

3. Results and Discussion

According to the XRD patterns of Figure 1, a series of Co-doped PBCFC-x ($x = 0, 2, 4, 6, 8$) demonstrate a well-crystallized phase of perovskite. The diffraction peaks of PBCFC-x reveal a tetragonal phase with a space group of P4mmm, proving that there was no phase

change after Co doping [40,44,45]. As can be seen, the peak positions of PBCFC-*x* shift to the right since element Co is doped, indicating a contraction in lattice volume. The positive movement of the PBCFC-*x* diffraction peak can be directly traced to the position of the Fe³⁺/Fe⁴⁺ (0.645/0.585 Å) occupied by the Co³⁺/Co⁴⁺ (0.615/0.53 Å) with a smaller ionic radius. The refinement profile and pertinent crystalline parameters for the as-prepared PBCFC-*x* (*x* = 0, 2, 4, 6, 8) samples analyzed using the Rietveld method are shown in Figure S1 and Table S1, respectively. The lattice parameters obtained from the refinement correspond to the XRD data obtained from the testing of the PBCFC-*x* (*x* = 0, 2, 4, 6, 8) samples. The trend of cell volume reduction of the above Co-doped samples coincides well with the positive shift of its peak position.

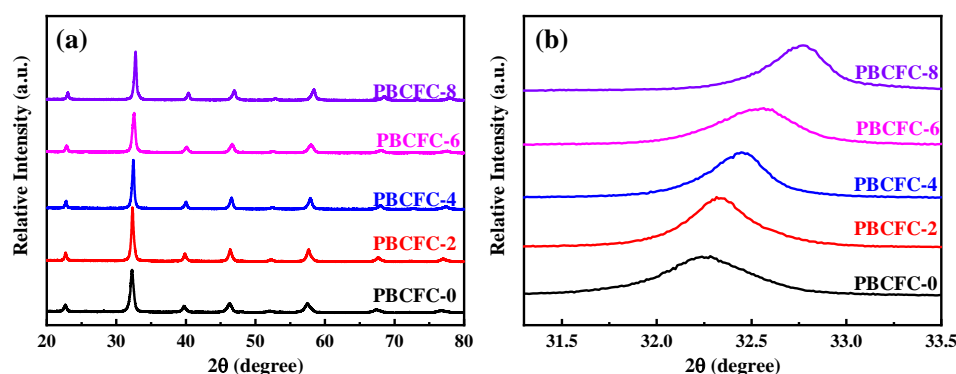


Figure 1. XRD patterns of PBCFC-*x* (*x* = 0, 2, 4, 6, 8) (a), their magnified diffraction peaks (b).

SEM images of PBCFC-*x* (*x* = 0, 2, 4, 6, 8) powder samples were employed to identify its morphology since there is a meaningful relationship between the quantity of its catalytically active sites and its particle size. As can be seen in Figure 2, all samples were not uniform in size and partial agglomerates, with the most pronounced agglomeration occurring in PBCFC-0. Furthermore, the Scherrer Equation was employed to analyze the XRD images of PBCFC-0, PBCFC-2, PBCFC-4, PBCFC-6, and PBCFC-8, which resulted in average particle sizes of 0.14 nm, 0.19 nm, 0.19 nm, 0.15 nm, and 0.24 nm, respectively. Although the Co-doped sample had slightly larger sizes, the significantly reduced particle aggregation of PBCFC-*x* means that its higher number of active sites undoubtedly facilitates the OER/ORR reaction. According to Figure S3, the specific surface areas of PBCFC-*x* (*x* = 0, 2, 4, 6, 8) were 7.4475, 7.7625, 7.76154, 7.7925, and 6.5804 m²·g⁻¹, respectively, which are in high agreement with the results of Scherrer Equation calculation as well as the SEM observations. According to Figure S2, the successful doping of element Co in PBCFC-*x* is revealed by the relatively homogeneous distribution of each element in the EDS pattern.

Rotating disk electrode technique measurements were carried out in O₂-saturated 0.1 M KOH solutions to assess the ORR electrocatalytic performance of PBCFC-*x* (*x* = 0, 2, 4, 6, 8) samples with different Co contents. The Linear scanning voltammetry (LSV) curves of various catalyst samples at 1600 rpm were compared to evaluate their ORR catalytic performance, as shown in Figure 3a. In comparison to other catalyst materials with various Co compositions, the onset potential of PBCFC-6 is significantly shifted in a more positive direction. The half-wave potential of the as-prepared catalyst materials follows the order of PBCFC-6 (0.59 V vs. RHE) > PBCFC-8 (0.568 V vs. RHE) > PBCFC-4 (0.566 V vs. RHE) > PBCFC-2 (0.563 V vs. RHE) > PBCFC-0 (0.524 V vs. RHE). Furthermore, PBCFC-6 possesses the highest limiting current density when compared to other materials, which means that the right amount of Co doping helps increase the ORR catalytic activity. As shown in Figure 3b, the electron transfer pathway of perovskites doped with different Co components was further investigated by fitting LSV pictures (Figure S3) over a range of different speeds (225–2500 rpm) using a K–L equation. Apparently, the values of electrons transferred by Co-doped PBCFC-2 (3.92), PBCFC-4 (3.72), PBCFC-6 (3.83), and PBCFC-8 (3.75) were closer to four relative to the 2.78 of PBCFC-0, demonstrating that a four-electron

dominated pathway to reduce oxygen to OH^- in the ORR is more likely to be used when Fe is partially replaced with Co in perovskite oxides [46,47].

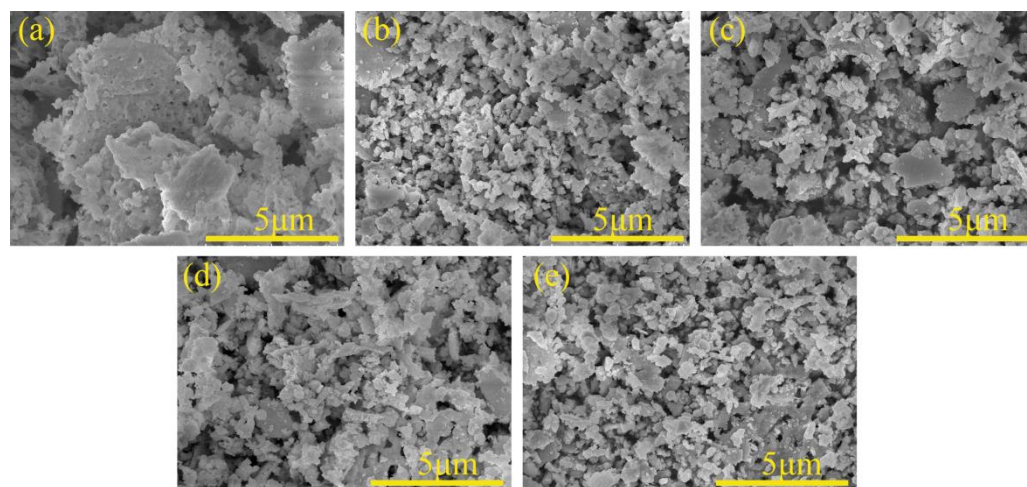


Figure 2. SEM images of PBCFC-0 (a), PBCFC-2 (b), PBCFC-4 (c), PBCFC-6 (d), and PBCFC-8 (e) samples.

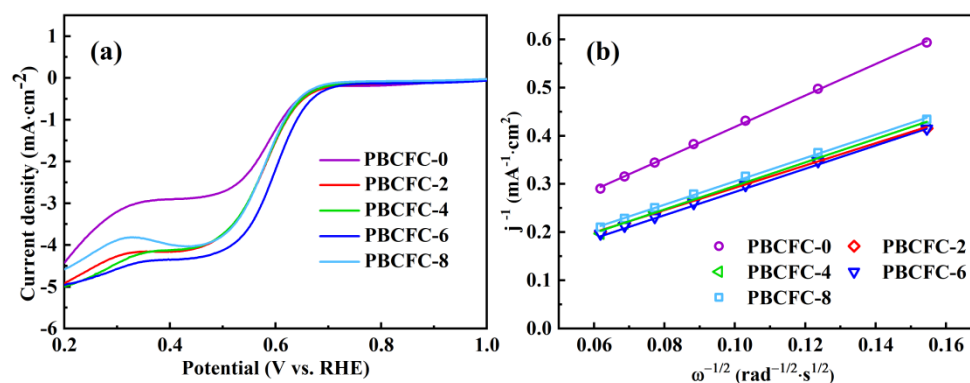


Figure 3. ORR polarization curves of PBCFC- x ($x = 0, 2, 4, 6, 8$) at 1600 rpm (a); The value of electrons transferred for PBCFC- x ($x = 0, 2, 4, 6, 8$) at 0.4 V vs. RHE (b).

To explore more about the bifunctional performance of PBCFC- x ($x = 0, 2, 4, 6, 8$) catalysts, the OER catalytic activity of the prepared materials was examined in 0.1 M O_2 -saturated KOH solution by LSVs at 1600 rpm. It is worth mentioning that PBCFC-6 had the lowest potential (1.621 V vs. RHE) among other materials at a current density of $10\text{mA}\cdot\text{cm}^{-2}$ and was lower than the 1.63 V vs. RHE of precious metal material RuO_2 (Figure 4). The overpotentials (η) of PBCFC-0, PBCFC-2, PBCFC-4, PBCFC-6, and PBCFC-8 were 439 mV, 415 mV, 415 mV, 391 mV, and 408 mV, respectively. As shown in Figure 4, the kinetics toward the OER activity of perovskites doped with different Co components were further investigated by the Tafel plot. The Tafel slopes of OER for PBCFC-0, PBCFC-2, PBCFC-4, PBCFC-6, and PBCFC-8 were 89, 89, 87.3, 85.7, and $96\cdot\text{dec}^{-1}\text{mV}\cdot\text{dec}^{-1}$, respectively. The minimum Tafel slopes of PBCFC-6 responded to the significant increase in OER intrinsic activity following Co doping. The PBCFC-6 had the lowest polarization resistance, as seen in Figure 4c, which highlights its improved capacity for charge transfer during the OER [48]. Figure S3 depicts CV curves for various scan speeds ($20\text{--}120\text{mV}\cdot\text{s}^{-1}$) in the non-Faraday region, and from this, the double-layer capacitance (C_{dl}) values were calculated for perovskite materials with different Co-doping compositions. The obtained C_{dl} of PBCFC-0, PBCFC-2, PBCFC-4, PBCFC-6, and PBCFC-8 were $2.6\text{mF}\cdot\text{cm}^{-2}$, $2.29\text{mF}\cdot\text{cm}^{-2}$, $2.69\text{mF}\cdot\text{cm}^{-2}$, $4.49\text{mF}\cdot\text{cm}^{-2}$, and $3.9\text{mF}\cdot\text{cm}^{-2}$, respectively. The maximum C_{dl} of PBCFC-

6 demonstrates a wider electrochemically active surface area (ECSA), which undoubtedly helped strengthen the efficiency of OER. As can be seen in Figures S5 and S6, the amperometric $i-t$ curve and CV tests were utilized to verify the OER stability of the PBCFC-0 and PBCFC-6. The overpotentials (η) of the PBCFC-6 diminish by just 13 mV after 500 CV tests and does not continue to decay after 1000 cycles when compared to the undoped PBCFC-0. The amperometric $i-t$ curve of the two materials also demonstrates the significance of Co doping in improving the OER stability of PBCFC-x.

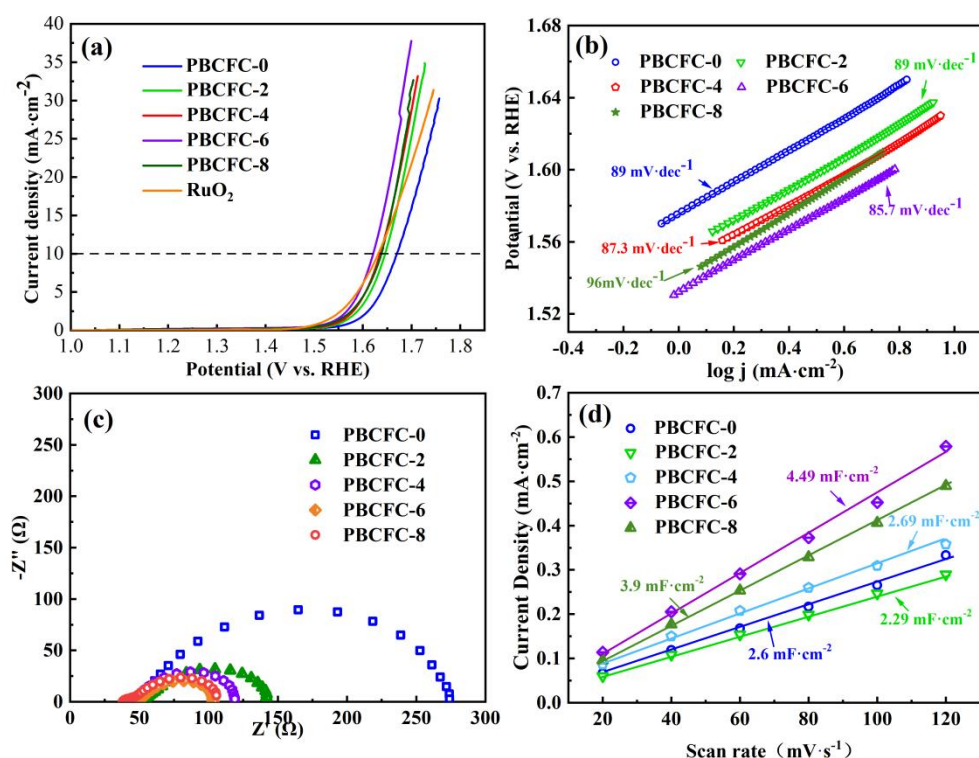


Figure 4. OER polarization profiles (1600 rpm) of PBCFC-x ($x = 0, 2, 4, 6, 8$) perovskites (a); The Tafel slope derived from the OER plots (b); The EIS at 0.6 V vs. SCE (c); The function of different scan rates and the current densities at 0.25 V vs. SCE for the PBCFC-x ($x = 0, 2, 4, 6, 8$) materials (d).

The bifunctional catalytic activity of the as-prepared PBCFC-x ($x = 0, 2, 4, 6, 8$) was evaluated by calculating the difference (ΔE) between the half-wave potential and $10 \text{ mA}\cdot\text{cm}^{-2}$ in the LSV curves of the ORR and OER. As shown in Table S2, the bifunctional catalytic performance of as-prepared catalyst materials follows the order of PBCFC-6 ($\Delta E = 1.03 \text{ V}$) > PBCFC-8 ($\Delta E = 1.06 \text{ V}$) > PBCFC-4 ($\Delta E = 1.07 \text{ V}$) > PBCFC-2 ($\Delta E = 1.08 \text{ V}$) > PBCFC-0 ($\Delta E = 1.14 \text{ V}$). Particularly, PBCFC-6 exhibits the best bifunctional catalytic activity in alkaline media among several materials and even can compare to the noble metal catalyst Pt/C ($\Delta E = 1 \text{ V}$), according to research using the rotating disk electrode technique.

The surface oxygen species and the transition metal ion state of PBCFC-0 and PBCFC-6 were examined by XPS since there is a significant relationship between the catalytic activity of OER/ORR and the chemical makeup on the surface of the perovskite. The survey spectrum of the as-prepared PBCFC-6 reveals clear Pr 3d, C 1s, Co 2p and Ba 3d, O 1s, Ca 3d, and Fe 2p peaks, as illustrated in Figure 5a. The O 1s spectra were deconvoluted into four distinct diffraction peaks, A (lattice oxygen species, O^{2-}), B (highly oxidative oxygen, $\text{O}_2^{2-}/\text{O}^-$), C (surface adsorbed oxygen/hydroxyl groups, O_2/OH^-), and D (molecular water/carbonates, $\text{H}_2\text{O}/\text{CO}_3^{2-}$) [49,50]. By fitting the peak areas, it was revealed that PBCFC-6 represented a comparatively higher amount of adsorbed oxygen, which will contribute to increasing the strength of the B-O bond and thus speeding up the rate-limiting $\text{O}_2^{2-}/\text{OH}^-$ substitution and OH^- regeneration during the ORR [51]. Accordingly, it is

predicted that the improved $\text{O}_2^{2-}/\text{OH}^-$ percentage in PBCFC-6 will have a positive effect on ORR efficiency. Additionally, the rising hydroxyl oxygen concentration encourages the chemisorbed OOH^- formation during the OER process, thus boosting its OER catalytic efficiency. Compared to PBCFC-0 (18.3%), the relatively higher proportion of adsorbed surface water of PBCFC-6 (21.1%) means that it is more hydrophilic, which facilitates better wettability of the catalyst sample with the electrolyte, thus positively affecting the OER/ORR performance [52].

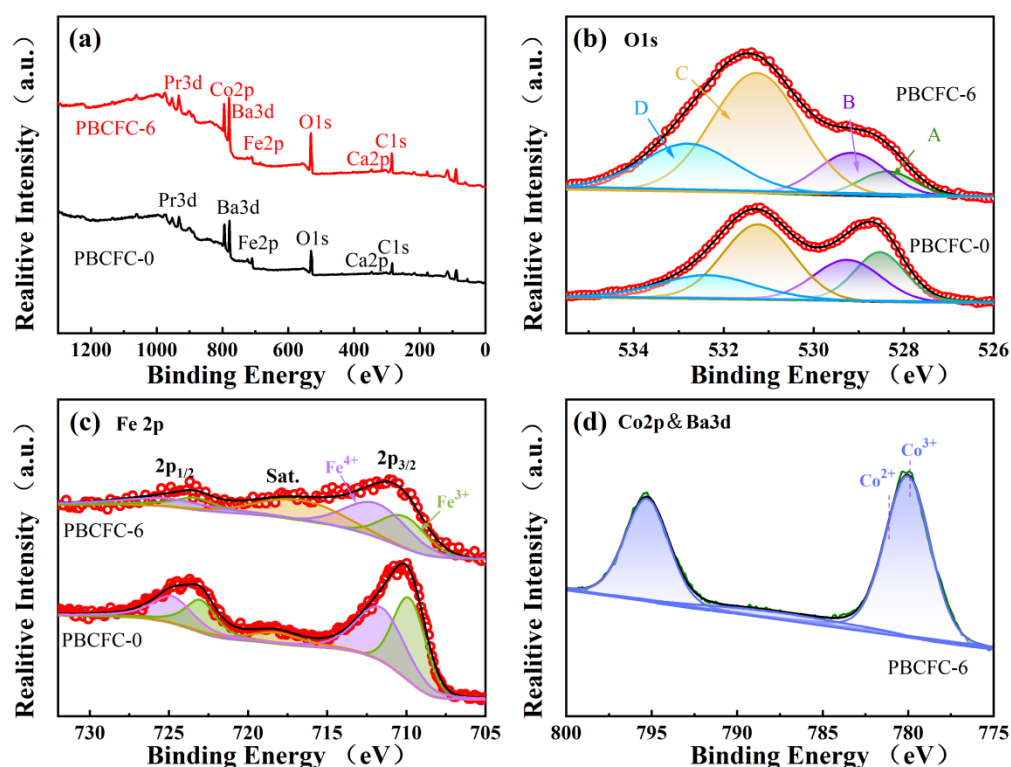


Figure 5. Full spectrum spectra (a), O 1s (b), Fe 2p (c), and Co 2p and Ba 3d spectrum (d) of PBCFC- x ($x = 0, 2, 4, 6, 8$) powders.

Upon deconvolution, the presence of Fe^{4+} and Fe^{3+} was confirmed to be around 711.86 and 710.14 eV in the Fe 2 $p_{3/2}$ region of the spectrum [53]. The percentages of Fe^{4+} for PBCFC-0 and PBCFC-6 were determined to be 52.8% and 59.8% by calculating the regions of the peaks separately. Given the optimal e_g orbital filling ($t_{2g}^3e_g^1$) of Fe^{4+} , the slightly increased amount of Fe^{4+} ions in PBCFC-6 is estimated to lead to improved OER properties [52–56]. As shown in Figure 5d, the peaks of Ba3d and Co2p overlapped heavily in their spectra due to their very close positions, while some previous reports have confirmed the presence of Co^{3+} and Co^{2+} to be around 779.7 eV and 781.1 eV, respectively [34]. Therefore, the presence of Co^{3+} ions in PBCFC-6 is also estimated to positively affect the OER/ORR performance owing to the optimal e_g orbital filling of Co^{3+} [22,55].

Numerous catalysts' bifunctional catalytic activity in 0.1 M KOH solution was characterized by RDE, and a homemade zinc–air cell operating at room temperature was used to evaluate both the stability and catalytic performance of these materials in practical working conditions. A primary zinc–air battery's working mechanism is depicted in Figure 6a. For a homemade primary zinc–air battery, the electrolyte and negative electrode are a 6M KOH solution and zinc powder pressed into flakes, respectively. The power density and LSV curves for the primary zinc–air batteries using PBCFC- x as the air cathode catalyst are depicted in Figure 6b. The maximum power densities of PBCFC-0, PBCFC-2, PBCFC-4, PBCFC-6, and PBCFC-8 were 55.85, 67.1, 66.33, 74.76, and 62.68 $\text{mW}\cdot\text{cm}^{-2}$, respectively. As is noticeable, PBCFC-6 exhibited the best ORR performance among several perovskite

materials with a peak power density 1.34 times greater than that of undoped PBCFC-0. To assess the cathode's performance when using various materials as catalysts, EIS was measured at a cell voltage of 1 V. To further investigate the reasons for the improved performance of the Co-doped catalysts, their impedance spectra were fitted separately by Zview. Figure 6c illustrates the equivalent circuit's five parts: R_s , R_{ct} , R_{int} , Q_{dl} , and Q_{int} , where Q_{int} and Q_{dl} stand for the capacitances produced by the electrode–electrolyte interface [56]. R_s is associated with the concentration of the electrolyte and the distance between the positive and negative electrodes, which corresponds to the electrolyte and contact resistance. The R_{int} and R_{ct} are defined as the solid electrolyte interface resistance and the air electrode charge transfer impedance, respectively [57]. Table 1 lists the aforementioned parameters that were obtained through fitting. Since the electrolyte and positive and negative pole spacing in the tests were similar, PBCFC-x had a relatively similar ohmic resistance of around 0.88. As R_{int} is tightly dependent on the intrinsic conductivity of the perovskite catalyst, we tested its conductivity at room temperature by the four-probe method. The conductivity of PBCFC-0, PBCFC-2, PBCFC-4, PBCFC-6, and PBCFC-8 were $8.931 \times 10^{-6} \text{ S}\cdot\text{cm}^{-1}$, $0.186 \text{ S}\cdot\text{cm}^{-1}$, $0.369 \text{ S}\cdot\text{cm}^{-1}$, $4.193 \text{ S}\cdot\text{cm}^{-1}$, and $2.945 \text{ S}\cdot\text{cm}^{-1}$. It was revealed that the appropriate Co doping increases the electrical conductivity of perovskite oxide significantly. In comparison to PBCFC-0 (0.31 Ω), the lower R_{int} of PBCFC-6 (0.20 Ω) benefits from its superior hydrophilicity, which corresponds to the relatively higher proportion of water adsorbed on its surface, as determined by XPS data. Among several materials, the zinc–air battery with PBCFC-6 as an air electrode catalyst possessed the smallest R_{ct} of 0.47, suggesting that it has a higher intrinsic ORR catalytic activity. Furthermore, the zinc–air battery with PBCFC-6 as a cathode catalyst had the lowest polarization resistance compared to any of the samples tested. As shown in Figure 6, the long-term output performance of primary zinc–air batteries with different materials as air electrode catalysts was tested at room temperature at a current density of $10 \text{ mA}\cdot\text{cm}^{-2}$. Obviously, the primary zinc–air batteries adopted PBCFC-x ($x = 2, 4, 6, 8$) as the air cathode catalyst displays a higher discharge voltage and discharge time than undoped PBCFC-0. In comparison to PBCFC-0, PBCFC-2, PBCFC-4 and PBCFC-8, the zinc–air battery utilizing PBCFC-6 as the air cathode catalyst expressed the greatest discharge voltage across the discharge process.

To realize the cycle capabilities of as-prepared perovskite oxides, a cycle (30 min for discharge, 30 min for charge, $10 \text{ mA}\cdot\text{cm}^{-2}$) experiment was carried out at room temperature for zinc–air batteries with different air electrode catalysts. For homemade rechargeable zinc–air batteries, the electrolyte and negative electrode are 6M KOH + 0.2 M acetate zinc solution and a 1 mm-thick polished zinc plate, respectively. Figure 7a,b presents the discharge cut-off voltage and charge cut-off voltage curves for the discharge–charge cycle of batteries with different perovskites as air cathode catalysts, respectively. Apparently, PBCFC-6 displays higher discharge voltages and lower charging voltages than the other four perovskites during the discharge–charge cycle test, demonstrating its superior energy efficiency. The variation of the discharge–charge voltage difference during the cycle test for the batteries with PBCFC-x ($x = 0, 2, 4, 6, 8$) as the oxygen electrode catalysts was shown in Table S3 where ΔE_1 , ΔE_{100} , and ΔE_d represent the difference in discharge–charge cut-off voltage for the first cycle, the 100th cycle, and the difference between them, respectively. In comparison with other materials, PBCFC-6 possessed a lower ΔE_1 of 0.827 V, which corresponds to its excellent ORR and OER activity. As shown in Figure 7, the voltage difference after 220 cycles (220 h) of batteries with PBCFC-6 as the oxygen electrode catalyst was 0.861 V, an increase of only 0.031 V compared to the first cycle, demonstrating the superior stability of PBCFC-6. Table S4 shows a comparison of the cycle life of PBCFC-x and other published materials used as cathode catalysts for zinc–air batteries. The comparison with previous materials indicated that PBCFC-6 is a durable cathode catalyst. All the above studies show that Co-doped PBCFC-6 possesses excellent bifunctional catalytic activity as well as high stability and might be an efficacious bifunctional catalyst.

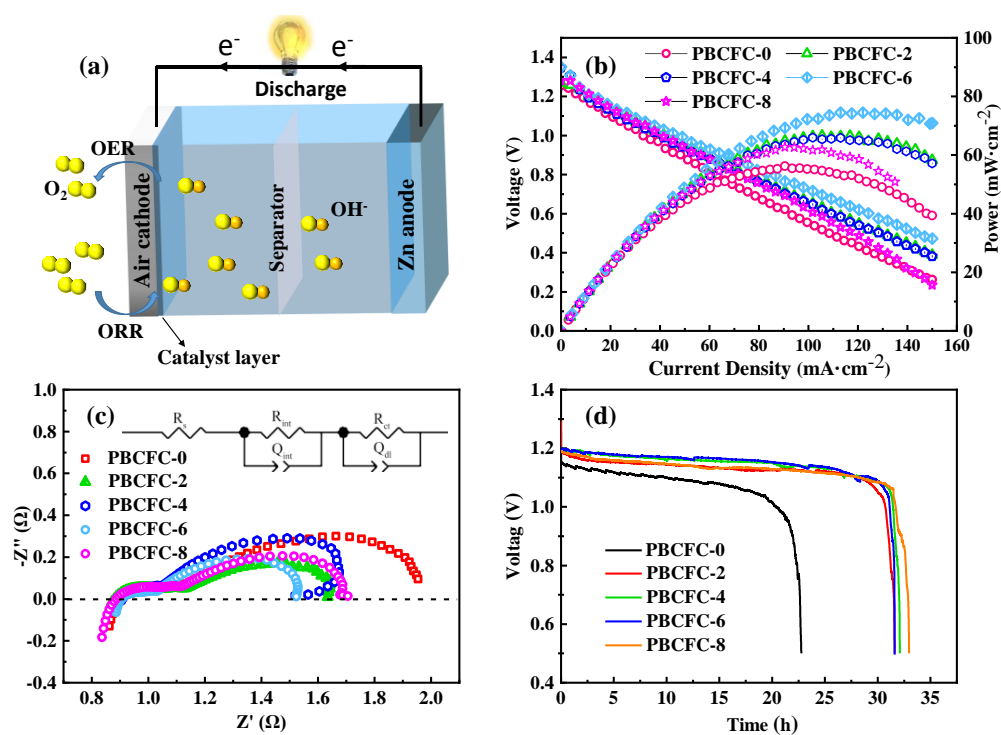


Figure 6. Diagram of the mechanism of a zinc–air battery (a); The power density and LSV profiles (b); Nyquist plots at 1 V vs. zinc (c); Discharge curves (10 mA·cm⁻²) (d) of zinc–air batteries with the PBCFC-x (x = 0, 2, 4, 6, 8) air electrode.

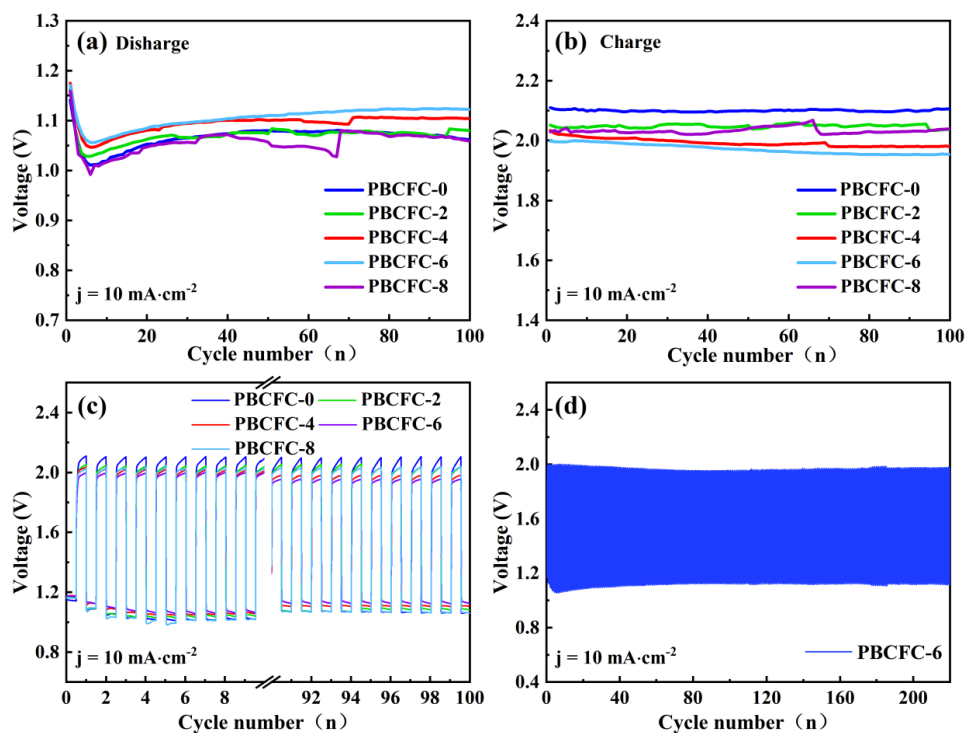


Figure 7. Constant current discharge cut-off voltage (a); Constant current charge cut-off voltage (b) of per cycle for a rechargeable zinc vacant battery with PBCFC-x as the oxygen electrode at 10 mA·cm⁻²; Comparison of cycling curves for PBCFC-x (c); Cycling curves for PBCFC-6 (d).

Table 1. The equivalent circuit components produced by the EIS values of PBCFC- x ($x = 0, 2, 4, 6, 8$).

Sample	R_S (Ω)	R_{int} (Ω)	R_{ct} (Ω)
PBCFC-0	0.89	0.31	0.83
PBCFC-2	0.88	0.30	0.55
PBCFC-4	0.88	0.27	0.69
PBCFC-6	0.89	0.20	0.47
PBCFC-8	0.87	0.28	0.58

4. Conclusions

In summary, a promising Co-doped $\text{Pr}_{0.5}\text{Ba}_{0.4}\text{Ca}_{0.1}\text{Fe}_{1-x}\text{Co}_x\text{O}_{3-\delta}$ ($x = 0, 2, 4, 6, 8$) is presented and used in zinc–air batteries as an air electrode catalyst to verify its durability and ORR/OER electrocatalytic activity. As an air electrode catalyst for zinc–air batteries, PBCFC-6 demonstrated a higher peak power density ($74.76 \text{ mW}/\text{cm}^{-2}$) and longer cycle time than other materials, demonstrating its superior bifunctional catalytic activity and durability. The optimized electrochemical performance of both OER and ORR as well as stability in zinc–air batteries might result from the higher electrical conductivity, increasing concentration of adsorbed oxygen, and the greater proportion of Fe^{4+} with optimal electron occupancy, owing to the partial replacement of Fe with Co. All these results provide a reasonable strategy for designing more efficient and stable perovskite oxides as an air electrode catalyst for rechargeable zinc–air batteries.

Supplementary Materials: The following supporting information can be downloaded at: <https://www.mdpi.com/article/10.3390/batteries8120259/s1>, Figure S1: Rietveld refinement of X-ray powder diffraction pattern of PBCFC-0 (a), PBCFC-2 (b), PBCFC-4 (c), PBCFC-6 (d), PBCFC-8 (e) samples; Figure S2 EDX images of PBCFC-0 (a), PBCFC-2 (b), PBCFC-4 (c), PBCFC-6 (d), PBCFC-8 (e); Figure S3: The N_2 adsorption/desorption isotherms for PBCFC x ($x = 0, 2, 4, 6, 8$) catalysts. The inset shows the BET surface area for all perovskite materials; Figure S5: LSV curves for PBCFC-0 and PBCFC-6 catalysts before and after 500th and 1000th CV ($100 \text{ mV}\cdot\text{s}^{-1}$) cycles test; Figure S6: The amperometric i - t curve for PBCFC-0 and PBCFC-6 catalysts at an initial current of $10 \text{ mA}\cdot\text{cm}^{-2}$; Figure S7 SEM photographs of the zinc negative electrode before (a) and after (b–d) cyclic charging and discharging; Table S1: List of Calculated Lattice Parameters of PBCFC- x through a Rietveld Refinement Method; Table S2: the bifunctional catalytic activity of various materials; Figure S4: CV curves of PBCFC-0 (a), PBCFC-2 (b), PBCFC-4 (c), PBCFC-6 (d) and PSFM-8 (e) at scan rates from 20 to $100 \text{ mV}\cdot\text{s}^{-1}$ and linear fitting of the current density difference versus the scan rates at 1.25 vs. RHE; Table S3: The variation of the charge/discharge voltage difference during the cycle of a zinc–air battery with PBCFC- x as the oxygen electrode; Table S4: Cycle testing comparison of materials used as zinc air battery cathode catalysts in the literature [58–72].

Author Contributions: K.L.: Investigation, Validation, Data curation, Writing original draft, Writing—review & editing. Z.D.: Supervision, Conceptualization, Writing—review & editing. Z.L.: Supervision, Funding acquisition, Resources, Writing—review & editing. All authors have read and agreed to the published version of the manuscript.

Funding: This work is financially supported by the National Science Foundation of China (51872067).

Institutional Review Board Statement: Not applicable.

Informed Consent Statement: Not applicable.

Data Availability Statement: Not applicable.

Conflicts of Interest: The authors declare no conflict of interest.

References

1. Chu, S.; Majumdar, A. Opportunities and challenges for a sustainable energy future. *Nature* **2012**, *488*, 294–303. [[CrossRef](#)] [[PubMed](#)]
2. Zhu, Y.L.; Zhou, W.; Chen, Y.B.; Yu, J.; Liu, M.L.; Shao, Z.P. A High-Performance Electrocatalyst for Oxygen Evolution Reaction: $\text{LiCo}_{0.8}\text{Fe}_{0.2}\text{O}_2$. *Adv. Mater.* **2015**, *27*, 7150–7155. [[CrossRef](#)] [[PubMed](#)]

3. Chen, D.J.; Chen, C.; Baiyee, Z.M.; Shao, Z.P.; Ciucci, F. Nonstoichiometric Oxides as Low-Cost and Highly-Efficient Oxygen Reduction/Evolution Catalysts for Low-Temperature Electrochemical Devices. *Chem. Rev.* **2015**, *115*, 9869–9921. [[CrossRef](#)] [[PubMed](#)]
4. Kumar, Y.A.; Kumar, K.D.; Kim, H.J. Facile preparation of a highly efficient NiZn₂O₄-NiO anoflower composite grown on Ni foam as an advanced battery-type electrode material for high-performance electrochemical supercapacitors. *Dalton Trans.* **2020**, *49*, 3622–3629. [[CrossRef](#)] [[PubMed](#)]
5. Yedluri, A.K.; Kim, H.J. Wearable super-high specific performance supercapacitors using a honeycomb with folded silk-like composite of NiCo₂O₄ nanoplates decorated with NiMoO₄ honeycombs on nickel foam. *Dalton Trans.* **2018**, *47*, 15545–15554. [[CrossRef](#)]
6. Kumar, Y.A.; Kumar, K.D.; Kim, H.J. Reagents assisted ZnCo₂O₄ nanomaterial for supercapacitor application. *Electrochim. Acta* **2020**, *330*, 135261. [[CrossRef](#)]
7. Mola, B.A.; Pallavolu, M.R.; Al-Asbahi, B.A.; Noh, Y.; Jilcha, S.K.; Kumar, Y.A. Design and construction of hierarchical MnFe₂Ce₄@MnNiCe₄ nanosheets on Ni foam as an advanced electrode for battery-type supercapacitor applications. *J. Energy Storage* **2022**, *51*, 104542. [[CrossRef](#)]
8. Yoon, J.H.; Kumar, Y.A.; Sambasivam, S.; Hira, S.A.; Krishna, T.N.V.; Zeb, K.; Uddin, W.; Kumar, K.D.; Obaidat, I.M.; Kim, S.; et al. Highly efficient copper-cobalt sulfide nano-reeds array with simplistic fabrication strategy for battery-type supercapacitors. *J. Energy Storage* **2020**, *32*, 101988. [[CrossRef](#)]
9. Bruce, P.G.; Freunberger, S.A.; Hardwick, L.J.; Tarascon, J.M. Li-O₂ and Li-S batteries with high energy storage. *Nat. Mater.* **2012**, *11*, 19–29. [[CrossRef](#)]
10. Khan, Z.; Vagin, M.; Crispin, X. Can Hybrid Na-Air Batteries Outperform Nonaqueous Na-O₂ Batteries? *Adv. Sci.* **2020**, *7*, 1902866. [[CrossRef](#)]
11. Sun, W.; Liu, W.D.; Liu, Q.; Chen, Z.G. Advances in thermoelectric devices for localized cooling. *Chem. Eng. J.* **2022**, *450*, 138389. [[CrossRef](#)]
12. Hong, W.T.; Risch, M.; Stoerzinger, K.A.; Grimaud, A.; Suntivich, J.; Shao-Horn, Y. Toward the rational design of non-precious transition metal oxides for oxygen electrocatalysis. *Energy Environ. Sci.* **2015**, *8*, 1404–1427. [[CrossRef](#)]
13. Niu, Y.; Xiao, M.L.; Zhu, J.B.; Zeng, T.T.; Li, J.D.; Zhang, W.Y.; Su, D.; Yu, A.P.; Chen, Z.W. A “trimurti” heterostructured hybrid with an intimate CoO/CoxP interface as a robust bifunctional air electrode for rechargeable Zn-air batteries. *J. Mater. Chem. A* **2020**, *8*, 9177–9184. [[CrossRef](#)]
14. Wang, M.F.; Qian, T.; Zhou, J.Q.; Yan, C.L. An Efficient Bifunctional Electrocatalyst for a Zinc-Air Battery Derived from Fe/N/C and Bimetallic Metal-Organic Framework Composites. *ACS Appl Mater. Inter.* **2017**, *9*, 5213–5221. [[CrossRef](#)] [[PubMed](#)]
15. Qian, J.M.; Guo, X.S.; Wang, T.T.; Liu, P.T.; Zhang, H.; Gao, D.Q. Bifunctional porous Co-doped NiO nanoflowers electrocatalysts for rechargeable zinc-air batteries. *Appl. Catal. B-Environ.* **2019**, *250*, 71–77. [[CrossRef](#)]
16. Guo, S.J.; Zhang, S.; Sun, S.H. Tuning Nanoparticle Catalysis for the Oxygen Reduction Reaction. *Angew Chem. Int Ed.* **2013**, *52*, 8526–8544. [[CrossRef](#)] [[PubMed](#)]
17. Wang, H.J.; Yu, H.J.; Yin, S.L.; Xu, Y.; Li, X.N.; Yamauchi, Y.; Xue, H.R.; Wang, L. In situ coating of a continuous mesoporous bimetallic PtRu film on Ni foam: A nanoarchitected self-standing all-metal mesoporous electrode. *J. Mater. Chem. A* **2018**, *6*, 12744–12750. [[CrossRef](#)]
18. Zhou, Z.H.; Zaman, W.Q.; Sun, W.; Cao, L.M.; Tariq, M.; Yang, J. Cultivating crystal lattice distortion in IrO₂ via coupling with MnO₂ to boost the oxygen evolution reaction with high intrinsic activity. *Chem. Commun.* **2018**, *54*, 4959–4962. [[CrossRef](#)] [[PubMed](#)]
19. Lee, Y.; Suntivich, J.; May, K.J.; Perry, E.E.; Shao-Horn, Y. Synthesis and Activities of Rutile IrO₂ and RuO₂ Nanoparticles for Oxygen Evolution in Acid and Alkaline Solutions. *J. Phys. Chem. Lett.* **2012**, *3*, 399–404. [[CrossRef](#)] [[PubMed](#)]
20. Bick, D.S.; Kindsmuller, A.; Staikov, G.; Gunkel, F.; Muller, D.; Schneller, T.; Waser, R.; Valov, I. Stability and Degradation of Perovskite Electrocatalysts for Oxygen Evolution Reaction. *Electrochim. Acta* **2016**, *218*, 156–162. [[CrossRef](#)]
21. Xue, Y.J.; Miao, H.; Sun, S.S.; Wang, Q.; Li, S.H.; Liu, Z.P. (La_{1-x}Sr_x)_(0.98)MnO₃ perovskite with A-site deficiencies toward oxygen reduction reaction in aluminum-air batteries. *J. Power Sources* **2017**, *342*, 192–201. [[CrossRef](#)]
22. Miao, H.; Wang, Z.H.; Wang, Q.; Sun, S.S.; Xue, Y.J.; Wang, F.; Zhao, J.P.; Liu, Z.P.; Yuan, J.L. A new family of Mn-based perovskite (La_{1-x}Y_xMnO₃) with improved oxygen electrocatalytic activity for metal-air batteries. *Energy* **2018**, *154*, 561–570. [[CrossRef](#)]
23. Ashok, A.; Kumar, A.; Bhosale, R.R.; Almomani, F.; Malik, S.S.; Suslov, S.; Tarlochan, F. Combustion synthesis of bifunctional LaMO₃ (M = Cr, Mn, Fe, Co, Ni) perovskites for oxygen reduction and oxygen evolution reaction in alkaline media. *J. Electroanal. Chem.* **2018**, *809*, 22–30. [[CrossRef](#)]
24. Ge, X.M.; Goh, F.W.T.; Li, B.; Hor, T.S.A.; Zhang, J.; Xiao, P.; Wang, X.; Zong, Y.; Liu, Z.L. Efficient and durable oxygen reduction and evolution of a hydrothermally synthesized La(Co_{0.55}Mn_{0.45})_(0.99)O_{3-δ} nanorod/graphene hybrid in alkaline media. *Nanoscale* **2015**, *7*, 9046–9054. [[CrossRef](#)]
25. Prabu, M.; Ramakrishnan, P.; Ganesan, P.; Manthiram, A.; Shanmugam, S. LaTi_{0.65}Fe_{0.35}O_{3-δ} nanoparticle-decorated nitrogen-doped carbon nanorods as an advanced hierarchical air electrode for rechargeable metal-air batteries. *Nano Energy* **2015**, *15*, 92–103. [[CrossRef](#)]
26. Gupta, S.; Kellogg, W.; Xu, H.; Liu, X.; Cho, J.; Wu, G. Bifunctional Perovskite Oxide Catalysts for Oxygen Reduction and Evolution in Alkaline Media. *Chem.-Asian J.* **2016**, *11*, 10–21. [[CrossRef](#)]

27. Zhu, Y.L.; Zhou, W.; Chen, Z.G.; Chen, Y.B.; Su, C.; Tade, M.O.; Shao, Z.P. SrNb_{0.1}Co_{0.7}Fe_{0.2}O_{3-δ} Perovskite as a Next-Generation Electrocatalyst for Oxygen Evolution in Alkaline Solution. *Angew Chem. Int. Ed.* **2015**, *54*, 3897–3901. [[CrossRef](#)]
28. Hua, B.; Zhang, Y.Q.; Yan, N.; Li, M.; Sun, Y.F.; Chen, J.; Li, J.; Luo, J.L. The Excellence of Both Worlds: Developing Effective Double Perovskite Oxide Catalyst of Oxygen Reduction Reaction for Room and Elevated Temperature Applications. *Adv. Funct. Mater.* **2016**, *26*, 4106–4112. [[CrossRef](#)]
29. Li, P.Z.; Wei, B.; Lu, Z.; Wu, Y.Y.; Huang, X.Q.; Zhang, Y.H. In-situ reduction synthesis of La₂O₃/NiM-NCNTs (M = Fe, Co) as efficient bifunctional electrocatalysts for oxygen reduction and evolution reactions. *Int. J. Hydrog. Energy* **2018**, *43*, 21959–21968. [[CrossRef](#)]
30. Grimaud, A.; May, K.J.; Carlton, C.E.; Lee, Y.L.; Risch, M.; Hong, W.T.; Zhou, J.G.; Shao-Horn, Y. Double perovskites as a family of highly active catalysts for oxygen evolution in alkaline solution. *Nat. Commun.* **2013**, *4*, 2439. [[CrossRef](#)]
31. Sun, Q.; Dai, Z.Y.; Zhang, Z.B.; Chen, Z.L.; Lin, H.Q.; Gao, Y.; Chen, D.J. Double perovskite PrBaCo₂O_{5.5}: An efficient and stable electrocatalyst for hydrogen evolution reaction. *J. Power Sources* **2019**, *427*, 194–200. [[CrossRef](#)]
32. Bu, Y.F.; Jang, H.; Gwon, O.; Kim, S.H.; Joo, S.H.; Nam, G.; Kim, S.; Qin, Y.; Zhong, Q.; Kwak, S.K.; et al. Synergistic interaction of perovskite oxides and N-doped graphene in versatile electrocatalyst. *J. Mater. Chem. A* **2019**, *7*, 2048–2054. [[CrossRef](#)]
33. Zhu, Y.M.; Zhang, L.; Zhao, B.T.; Chen, H.J.; Liu, X.; Zhao, R.; Wang, X.W.; Liu, J.; Chen, Y.; Liu, M.L. Improving the Activity for Oxygen Evolution Reaction by Tailoring Oxygen Defects in Double Perovskite Oxides. *Adv. Funct. Mater.* **2019**, *29*, 1901783. [[CrossRef](#)]
34. Zhang, B.Z.; Wan, Y.H.; Hua, Z.H.; Tang, K.B.; Xia, C.R. Tungsten-Doped PrBaFe₂O_{5+δ} Double Perovskite as a High-Performance Electrode Material for Symmetrical Solid Oxide Fuel Cells. *ACS Appl. Energ. Mater.* **2021**, *4*, 8401–8409. [[CrossRef](#)]
35. Kim, G.; Wang, S.; Jacobson, A.J.; Reimus, L.; Brodersen, P.; Mims, C.A. Rapid oxygen ion diffusion and surface exchange kinetics in PrBaCo₂O_{5+x} with a perovskite related structure and ordered A cations. *J. Mater. Chem.* **2007**, *17*, 2500–2505. [[CrossRef](#)]
36. Wu, Z.L.; Sun, L.P.; Xia, T.; Huo, L.H.; Zhao, H.; Rougier, A.; Grenier, J.C. Effect of Sr doping on the electrochemical properties of bi-functional oxygen electrode PrBa_{1-x}Sr_xCo₂O_{5+δ}. *J. Power Sources* **2016**, *334*, 86–93. [[CrossRef](#)]
37. Bu, Y.F.; Gwon, O.; Nam, G.; Jang, H.; Kim, S.; Zhong, Q.; Cho, J.; Kim, G. A Highly Efficient and Robust Cation Ordered Perovskite Oxide as a Bifunctional Catalyst for Rechargeable Zinc-Air Batteries. *ACS Nano* **2017**, *11*, 11594–11601. [[CrossRef](#)]
38. He, D.D.; He, G.G.; Jiang, H.Q.; Chen, Z.K.; Huang, M.H. Enhanced durability and activity of the perovskite electrocatalyst Pr_{0.5}Ba_{0.5}CoO_{3-δ} by Ca doping for the oxygen evolution reaction at room temperature. *Chem. Commun.* **2017**, *53*, 5132–5135. [[CrossRef](#)]
39. Li, X.N.; Zhang, J.; Feng, Q.; Pu, C.Y.; Zhang, L.Z.; Hu, M.M.; Zhou, X.Y.; Zhong, X.W.; Yi, W.D.; Tang, J.; et al. Redox inactive ion meliorated BaCo_{0.4}Fe_{0.4}Zr_{0.1}Y_{0.1}O_{3-δ} perovskite oxides as efficient electrocatalysts for the oxygen evolution reaction. *J. Mater. Chem. A* **2018**, *6*, 17288–17296. [[CrossRef](#)]
40. He, W.; Wu, X.L.; Dong, F.F.; Ni, M. A novel layered perovskite electrode for symmetrical solid oxide fuel cells: PrBa(Fe_{0.8}Sc_{0.2})₂O_{5+δ}. *J. Power Sources* **2017**, *363*, 16–19. [[CrossRef](#)]
41. Hua, B.; Sun, Y.F.; Li, M.; Yan, N.; Chen, J.; Zhang, Y.Q.; Zeng, Y.M.; Amirkhiz, B.S.; Luo, J.L. Stabilizing Double Perovskite for Effective Bifunctional Oxygen Electrocatalysis in Alkaline Conditions. *Chem. Mater.* **2017**, *29*, 6228–6237. [[CrossRef](#)]
42. Li, P.Z.; Wei, B.; Lu, Z.; Wu, Y.Y.; Zhang, Y.H.; Huang, X.Q. La_{1.7}Sr_{0.3}Co_{0.5}Ni_{0.5}O_{4+δ} layered perovskite as an efficient bifunctional electrocatalyst for rechargeable zinc-air batteries. *Appl. Surf. Sci.* **2019**, *464*, 494–501. [[CrossRef](#)]
43. Li, K.X.; Dong, Z.H.; Lue, Z. Study of the bifunctional catalytic activity on Sr and Mn co-doped PrFeO_{3-δ} Zinc-Air batteries cathode. *Electrochim. Acta* **2022**, *430*, 141123. [[CrossRef](#)]
44. Lim, C.; Sengodan, S.; Jeong, D.; Shin, J.; Kim, G. Investigation of the Fe doping effect on the B-site of the layered perovskite PrBa_{0.8}Ca_{0.2}Co₂O_{5+δ} for a promising cathode material of the intermediate-temperature solid oxide fuel cells. *Int. J. Hydrog. Energy* **2019**, *44*, 1088–1095. [[CrossRef](#)]
45. Lu, C.L.; Niu, B.B.; Yi, W.D.; Ji, Y.; Xu, B.M. Efficient symmetrical electrodes of PrBaFe_{2-x}Co_xO_{5+δ} (x=0, 0.2, 0.4) for solid oxide fuel cells and solid oxide electrolysis cells. *Electrochim. Acta* **2020**, *358*, 136916. [[CrossRef](#)]
46. Ge, X.M.; Sumboja, A.; Wu, D.; An, T.; Li, B.; Goh, F.W.T.; Hor, T.S.A.; Zong, Y.; Liu, Z.L. Oxygen Reduction in Alkaline Media: From Mechanisms to Recent Advances of Catalysts. *ACS Catal.* **2015**, *5*, 4643–4667. [[CrossRef](#)]
47. Waidha, A.I.; Ni, L.M.; Ali, J.; Lepple, M.; Donzelli, M.; Dasgupta, S.; Wollstadt, S.; Alff, L.; Kramm, U.I.; Clemens, O. Synthesis of bifunctional BaFe_{1-x}Co_xO_{3-y-δ}(OH)_(y) catalysts for the oxygen reduction reaction and oxygen evolution reaction. *J. Mater. Chem. A* **2020**, *8*, 616–625. [[CrossRef](#)]
48. Lee, D.; Lee, H.; Gwon, O.; Kwon, O.; Jeong, H.Y.; Kim, G.; Lee, S.Y. Monolithic heteronanomat paper air cathodes toward origami-foldable/rechargeable Zn-air batteries. *J. Mater. Chem. A* **2019**, *7*, 24231–24238. [[CrossRef](#)]
49. Wang, H.C.; Zhang, W.W.; Guan, K.; Wei, Z.Y.; Meng, J.L.; Meng, J.; Liu, X.J. Enhancing Activity and Durability of A-Site-Deficient (La_{0.6}Sr_{0.4})_(0.95)Co_{0.2}Fe_{0.8}O_{3-δ} Cathode by Surface Modification with Pr_{2-δ} Nanoparticles. *Acs Sustain. Chem. Eng.* **2020**, *8*, 3367–3380. [[CrossRef](#)]
50. Li, Z.S.; Lv, L.; Wang, J.S.; Ao, X.; Ruan, Y.J.; Zha, D.C.; Hong, G.; Wu, Q.H.; Lan, Y.C.; Wang, C.D.; et al. Engineering phosphorus-doped LaFeO_{3-δ} perovskite oxide as robust bifunctional oxygen electrocatalysts in alkaline solutions. *Nano Energy* **2018**, *47*, 199–209. [[CrossRef](#)]
51. Zhu, Y.L.; Lin, Q.; Wang, Z.B.; Qi, D.C.; Yin, Y.C.; Liu, Y.; Zhang, X.W.; Shao, Z.P.; Wang, H.T. Chlorine-anion doping induced multi-factor optimization in perovskites for boosting intrinsic oxygen evolution. *J. Energy Chem.* **2021**, *52*, 115–120. [[CrossRef](#)]

52. Zhang, D.W.; Song, Y.F.; Du, Z.Z.; Wang, L.; Li, Y.T.; Goodenough, J.B. Active $\text{LaNi}_{1-x}\text{Fe}_x\text{O}_3$ bifunctional catalysts for air cathodes in alkaline media. *J. Mater. Chem. A* **2015**, *3*, 9421–9426. [[CrossRef](#)]
53. Zhu, Y.L.; Zhou, W.; Yu, J.; Chen, Y.B.; Liu, M.L.; Shao, Z.P. Enhancing Electrocatalytic Activity of Perovskite Oxides by Tuning Cation Deficiency for Oxygen Reduction and Evolution Reactions. *Chem. Mater.* **2016**, *28*, 1691–1697. [[CrossRef](#)]
54. She, S.X.; Yu, J.; Tang, W.Q.; Zhu, Y.L.; Chen, Y.B.; Sunarso, J.; Zhou, W.; Shao, Z.P. Systematic Study of Oxygen Evolution Activity and Stability on $\text{La}_{1-x}\text{Sr}_x\text{FeO}_{3-\delta}$ Perovskite Electrocatalysts in Alkaline Media. *ACS Appl. Mater. Inter.* **2018**, *10*, 11715–11721. [[CrossRef](#)] [[PubMed](#)]
55. Mondal, R.; Ratnawat, H.; Mukherjee, S.; Gupta, A.; Singh, P. Investigation of the Role of Sr and Development of Superior Sr-Doped Hexagonal $\text{BaCoO}_{3-\delta}$ Perovskite Bifunctional OER/ORR Catalysts in Alkaline Media. *Energ. Fuel* **2022**, *36*, 3219–3228. [[CrossRef](#)]
56. Chen, Z.; Yu, A.P.; Higgins, D.; Li, H.; Wang, H.J.; Chen, Z.W. Highly Active and Durable Core-Corona Structured Bifunctional Catalyst for Rechargeable Metal-Air Battery Application. *Nano Lett.* **2012**, *12*, 1946–1952. [[CrossRef](#)]
57. Lee, D.U.; Choi, J.Y.; Feng, K.; Park, H.W.; Chen, Z.W. Advanced Extremely Durable 3D Bifunctional Air Electrodes for Rechargeable Zinc-Air Batteries. *Adv. Energy Mater.* **2014**, *4*, 1301389. [[CrossRef](#)]
58. Wang, Z.; You, Y.; Yuan, J.; Yin, Y.X.; Li, Y.T.; Xin, S.; Zhang, D. Nickel-Doped $\text{La}_{0.8}\text{Sr}_{0.2}\text{Mn}_{1-x}\text{Ni}_x\text{O}_3$ Nanoparticles Containing Abundant Oxygen Vacancies as an Optimized Bifunctional Catalyst for Oxygen Cathode in Rechargeable Lithium-Air Batteries. *ACS Appl. Mater. Interfaces* **2016**, *8*, 6520–6528. [[CrossRef](#)]
59. Yan, L.; Lin, Y.; Yu, X.; Xu, W.; Salas, T.; Smallidge, H.; Zhou, M.; Luo, H. $\text{La}_{0.8}\text{Sr}_{0.2}\text{MnO}_3$ -Based Perovskite Nanoparticles with the A-Site Deficiency as High Performance Bifunctional Oxygen Catalyst in Alkaline Solution. *ACS Appl. Mater. Interfaces* **2017**, *9*, 23820–23827. [[CrossRef](#)]
60. Wang, Z.; Jin, C.; Sui, J.; Li, C.; Yang, R. Phosphorus-doped $\text{SrCo}_{0.5}\text{Mo}_{0.5}\text{O}_3$ perovskites with enhanced bifunctional oxygen catalytic activities. *Int. J. Hydrogen Energy* **2018**, *43*, 20727–20733. [[CrossRef](#)]
61. Bian, J.; Su, R.; Yao, Y.; Wang, J.; Zhou, J.; Li, F.; Wang, Z.L.; Sun, C. Mg Doped Perovskite LaNiO_3 Nanofibers as an Efficient Bifunctional Catalyst for Rechargeable Zinc-Air Batteries. *ACS Appl. Energy Mater.* **2019**, *2*, 923–931. [[CrossRef](#)]
62. Zhao, C.X.; Liu, J.N.; Yao, N.; Wang, J.; Ren, D.; Chen, X.; Li, B.Q.; Zhang, Q. Can Aqueous Zinc-Air Batteries Work at Sub-Zero Temperatures? *Angew. Chem. Int. Edit.* **2021**, *60*, 15281–15285. [[CrossRef](#)]
63. Jiao, D.; Ma, Z.; Li, J.S.; Han, Y.J.; Mao, J.; Ling, T.; Qiao, S.Z. Test factors affecting the performance of zinc-air battery. *J. Energy Chem.* **2020**, *44*, 1–7. [[CrossRef](#)]
64. Yang, C.; Shang, S.S.; Gu, Q.F.; Shang, J.; Li, X.Y. Metal-organic framework-derived carbon nanotubes with multi-active Fe-N/Fe sites as a bifunctional electrocatalyst for zinc-air battery. *J. Energy Chem.* **2022**, *66*, 306–313. [[CrossRef](#)]
65. Ramakrishnan, S.; Velusamy, D.B.; Sengodan, S.; Nagaraju, G.; Kim, D.H.; Kim, A.R.; Yoo, D.J. Rational design of multifunctional electrocatalyst: An approach towards efficient overall water splitting and rechargeable flexible solid-state zinc-air battery. *Appl. Catal. B Environ.* **2022**, *300*, 120752. [[CrossRef](#)]
66. Li, Z.S.; Lv, L.; Ao, X.; Li, J.G.; Sun, H.C.; An, P.D.; Xue, X.Y.; Li, Y.; Liu, M.; Wang, C.D.; et al. An effective method for enhancing oxygen evolution kinetics of LaMO_3 (M = Ni, Co, Mn) perovskite catalysts and its application to a rechargeable zinc-air battery. *Appl. Catal. B-Environ.* **2020**, *262*, 118291. [[CrossRef](#)]
67. Wang, X.X.; Sunarso, J.; Lu, Q.; Zhou, Z.L.; Dai, J.; Guan, D.Q.; Zhou, W.; Shao, Z.P. High-Performance Platinum-Perovskite Composite Bifunctional Oxygen Electrocatalyst for Rechargeable Zn-Air Battery. *Adv. Energy Mater.* **2020**, *10*, 1903271. [[CrossRef](#)]
68. Wu, X.Y.; Miao, H.; Hu, R.G.; Chen, B.; Yin, M.M.; Zhang, H.C.; Xia, L.; Zhang, C.F.; Yuan, J.L. A-site deficient perovskite nanofibers boost oxygen evolution reaction for zinc-air batteries. *Appl. Surf. Sci.* **2021**, *536*, 147806. [[CrossRef](#)]
69. Yuan, R.H.; Chen, B.; Zhang, Y.; Tan, F.R.; Liu, T. Boosting the bifunctional electrocatalytic activity of cobalt free perovskite oxide ($\text{La}_{0.8}\text{Sr}_{0.2}$)(0.95) MnO_3 via iron doping for high-efficiency Zn-air batteries. *Sep. Purif. Technol.* **2022**, *300*, 121858. [[CrossRef](#)]
70. Lin, H.Q.; Xie, J.; Zhang, Z.B.; Wang, S.F.; Chen, D.J. Perovskite nanoparticles@N-doped carbon nanofibers as robust and efficient oxygen electrocatalysts for Zn-air batteries. *J. Colloid Interf. Sci.* **2021**, *581*, 374–384. [[CrossRef](#)]
71. Nie, R.G.; Deng, Y.Q.; Yang, H.; Tan, Y.; Yuan, H.B.; Sagar, R.U.R.; Liang, T.X. Efficient oxygen evolution reaction in $\text{SrCo}_{0.8}\text{Fe}_{0.2}\text{O}_{3-\delta}$ perovskite and surface reconstruction for practical zinc-air batteries. *Appl. Surf. Sci.* **2021**, *552*, 149509. [[CrossRef](#)]
72. Shi, X.J.; Deng, Y.Z.; Zhao, L.; Gong, Y.S.; Wang, R.; Wang, H.W.; He, B.B. In-situ photodeposition of CoS_x on $\text{Pa}_{0.5}\text{Ba}_{0.5}\text{Mn}_{0.25}\text{Fe}_{0.75}\text{O}_{3-\delta}$ perovskite to boost bifunctional oxygen electrocatalysis for rechargeable Zn-air batteries. *Electrochim. Acta.* **2021**, *391*, 138951. [[CrossRef](#)]